A numerical study of the rapid deflagration-to-detonation transition in a high-frequency pulse detonation engine

Yuqi Wang[1] (王玉奇), Jianhan Liang[1]* (梁剑寒), Ralf Deiterding[2], Xiaodong Cai[1]* (蔡晓东), Lin Zhang[1] (张林)

[1]Science and Technology on Scramjet Laboratory

National University of Defense Technology, Changsha, 410073, China

[2]Aerodynamics and Flight Mechanics Research Group, University of Southampton

Highfield Campus, Southampton SO171BJ, United Kingdom

*Corresponding author: jhleon@vip.sina.com

*Corresponding author: cai-chonger@hotmail.com

Abstract: This paper describes numerically the rapid deflagration-to-detonation transition (DDT) in detail in a high-frequency pulse detonation rocket engine (PDRE). Different from traditional DDT, reactants are injected into the chamber from near the open end and travel toward the closed end. Previous experiments have implied that the gas-dynamic shock by injecting in a confined space and the intensive turbulence generated by the high-speed jet play important roles in the detonation initiation, but explanations of how, when and where the detonation is generated were not presented clearly due to the limitation of experimental observation. In this work, high-resolution two-dimensional simulations are performed to investigate this process employing a physical model similar to the experimental configuration. A new mechanism manifesting itself as a complicated vortex-flame interaction is found for the flame transition from a laminar to a compressible or choking regime. And it is discovered that the gas-dynamic shock, after reflecting from the end wall, triggers the detonation through the gradient of reactivity with the hot spot formed by the collision of the shock and the flame. A dimensionless criterion defined by the ratio of the acoustic speed to the inverse gradient of the ignition delay time is applied to further describe the spontaneous wave propagation from the perspective of chem-physical dynamics. This criterion quantitatively gives a good prediction of the propagating mode from the subsonic deflagration to a developing detonation, even in such a complex scenario as encountered in this work.

1. Introduction

Recently, detonation has been especially focused in the propulsion area due to its intrinsic higher combustion efficiency as compared to deflagration [1-2]. Among detonation thrusters, the pulse detonation engine (PDE) was developed earlier for its simple configuration with the thrust generated by repeatedly initiating detonation waves [3]. Considering the difficulty in directly initiating the detonation, deflagration to detonation transition (DDT) is commonly recognized as a more practical way to obtain a detonation by accelerating the flame through a laminar to

the eventual detonable regime. And reducing the DDT run-up distance and time has always been a valuable but difficult problem.

A typical configuration of the detonation chambers is a half-confined channel with one end open. Detonations are usually developed from the head of the channel by an initial ignition and are discharged from the exit. To accelerate DDT, internal solid obstacles inside of the tube were first attempted to perturb the flame by generating shock-related interactions and flow instabilities [4-5]. Nevertheless, this would result in considerable total pressure losses, as reported by Cooper [6] who noted that solid obstacles can decrease the impulse by an average of 25% as compared with that for a smooth channel. Consequently, fluidic obstacles in the form of gas or liquid jets were proposed and widely investigated due to their superiority in minimizing flow losses. McGarry [7] and Knox [8] reported that the fluidic obstacles even generate more turbulence in the early stage of flame evolution than those solid obstacles with identical blockage ratios. On the other hand, however, those jet-supple devices to some degree complicate the engine controlling system by carrying additional plenum devices, as well as by periodical control of the opening/closing of jet valves. In smooth channels with submillimeter-scale heights (usually at the order of ~mm) [9], DDT is more likely to occur near the viscous wall due to the stretching and heating in the boundary layers. However, the onset of detonation is highly dependent on geometry, which means that detonation only occurs in cases where the boundary layers dominate the entire flow [10]. Besides, it was also reported [11] that extremely narrow channels can even restrain the growth of the detonation structure adversely when the height of the channel is less than one cell size of the cellular detonation. Thus, here raises the question of whether DDT can occur within a short distance and time in wide channels in the absence of internal obstacles.

End-gas autoignition is a particular combustion phenomenon by an incident shock or wave system traveling toward the end wall and inducing autoignition here after reflecting off and compressing the mixture again [12-13]. In shock-tube experiments [14-15], the incident shock is released through the driver section contained with high-

pressure inert gases while in simulation studies, this shock is simply specified by the Rankine-Hugoniot relations [16-17]. Several combustion modes were observed and verified in both experiments and simulations, determined primarily by the strength of the incident shock and temperature inhomogeneity by complex reflected shock-boundary layer interactions. Among these combustion modes with detonation emergence, the “weak ignition” mode [18], developed under a relatively weak incident shock, consists of first the autoignition of distributed flame kernels behind the reflective shock and thereafter transition to detonation by temperature inhomogeneity through the SWACER (shock wave amplification by coherent energy release) mechanisms. In this mode, detonation is generated by pure shock-boundary layer interactions and reactivity gradients without internal obstructions required. It differs from traditional DDTs in that the onset of detonation emerges near the closed end and the gas-dynamic shock is required to be strong enough or else the mixture would be not ignited or ignited in a deflagration mode. Considering the feasibility of generating such a strong gas-dynamic shock, this end-gas detonation initiation approach has not been systematically presented in PDEs.

In addition to gas-dynamic disturbances, thermal-dynamic waves generated during the unstable flame acceleration in smooth tubes are also studied in two- and three-dimensional simulations [19-21]. These waves were reported to be able to interact with the propagating flame after reflecting from the closed end and induce Rayleigh-Taylor-type instabilities amplifying the heat release rate of the flame. However, those studies came to a consistent conclusion that this kind of interaction is too weak to initiate a detonation. Zhao and Zhou et al [22-24] studied the “Super knock” phenomenon in a rapid compression machine by compression and reflection of thermo-dynamic waves emanating from the propagating flame, with a compressible deflagration flame produced rapidly accelerated by a constant-volume combustion bomb combined with a perforated plate. They also [25] conducted a 2D simulation on this similar question with the flame developed from a flame kernel. In their computations, the height of the tube is set on a millimeter scale and the initial mixture temperature and pressure before ignition reach up to 1000K and

10bars, respectively, which are far from the real conditions in detonation engines. The conditions they focused on are closer to those of the internal combustion engines (ICEs) instead of PDEs.

Previous numerical simulations concerned with DDT usually considered an initially homogeneous mixture in the tube [26-28], to isolate the flame deformation and evolution from complicated disturbances such as the uniformity of velocity and mass fractions. On the other hand, however, reactant supply may play an important part in pre-disturbing the flows before ignition, flame acceleration and detonation. Prior work [30-32] tended to assume the reactant injected at the head of the tube and filling toward the open end, but by setting like this, generating a gas-dynamic shock oscillated within the tube is difficult. Cutler and his co-workers [33-36] pioneeringly presented to facilitate DDT by injecting reactants from near the open end toward the closed end in their high-frequency pulse detonation rocket engine (PDRE) study, through which way the reactive gases injected into the tube are pre-heated by compression of the injection-driven shock reflected off the end wall. However, although a periodic pressure peak close to the CJ detonation pressure was observed, no convincing proof can further confirm the emergence of detonation for limited experimental results. In their most recent paper [37], it was noted that the pressure peak observed may be just a supersonic deflagration. In our opinion, the failed detonation is probably related to the inappropriate ignition method: In Cutler‘s experiments [37], fresh reactants were reported to be ignited by contact with the residual products from the last cycle. However, turbulence generated during the reactant injection and combustion makes it highly unpredictable exactly where and when the fresh gases meet with the hot products and thus are ignited, which is to be illustrated in the following text to impose a significant effect on the final combustion regime. Lu [38] performed similar research later but instead adopted a periodic position-fixed spark ignition. The successful detonation was reported in their experiments. Apart from that, possible promoting effects on DDT by the turbulence of the jet were also mentioned in Lu’s paper [38] but not further discussed and analyzed. To summarize, as discussed above, prior studies provide a possible path for rapid DDT by injecting reactants from the open end. For

lack of detailed description, some key steps about how the laminar flame evolves into a compressible flame and when and where the detonation is initiated exactly are still known.

The contribution of this work is to elucidate mechanistically the onset of detonation by a propagating flame interacting with a gas-dynamic shock produced by downstream fuel injection, thus illustrating a rapid DDT method. Besides, the formation of a CJ deflagration flame before the flame-shock interaction is evaluated in detail by recognizing a new-type flame-turbulence interaction. Differing from previous end-wall autoignition simulations, the fully-evolved flame is originated from a flame kernel initiated by a weak spark at a selected appropriate position and instant, and the gas-dynamic shock is produced by the indispensable fuel injection process, so the simulation results are trustworthy and physically feasible with no additional assumptions made.

The remainder of this paper is organized as follows: Section 2 introduces the physical model and some related mathematical derivations. Section 3 presents the computation setup, numerical schemes, and convergence analysis on grid resolutions. As the main innovation of this paper, Section 4 illustrates an untraditional rapid DDT process and the underlying mechanisms therein, with the transition of the combustion modes described further via a dimensionless number from the chemical physics perspective.

2. Physical model

A schematic diagram of the chamber configuration is shown in Fig. 1. The rectangular chamber length L_x and height L_y are 15 cm and 2 cm, respectively. The exit of the chamber is connected with a sufficiently large ambient air reservoir (not shown here), while the inside is initially filled with inert gases under 101.325 KPa and 300K to simulate the flow field after purging the residual products from the last detonation cycle away. For simplification, the inert media are set to be quiescent along the entire length of the channel, as the purging speed is usually negligible after the injection starts. The left side and the upper and lower boundaries are all set as adiabatic no-slip walls, with

an intermittent injection located on the bottom wall. As opposed to the usual injection from the closed end in traditional DDT studies, following Cutler [37], a stoichiometric hydrogen and oxygen-rich air (33% O_2 and 67% N_2 in mole fractions) mixture is injected into the chamber with a downward angle of 45 degrees from near the open end. In the experiments [33-38], a rotary valve is employed to meet the requirement of injection frequency and flow rates. To imitate the character of the rotary valve, a half sinusoidal waveform, as signaled by the red dashed line in arbitrary units in Fig. 2, is employed for simulating the opening width of the nozzle with a peak value d_0 of 1.5cm. Considering that in real situations the z-axis length of the chamber, L_z, usually equals the height L_y, the effective nozzle diameter d' shall be similar to d_0, which is comparable with the valve diameters employed in the experiments.

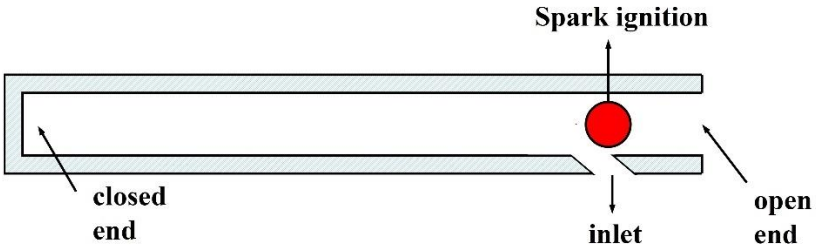

Fig. 1 Physical model of the 2D chamber

One of the key characteristics of injecting from the open end is the generation of gas-dynamic waves. The injection point could be regarded as a sound source adding mass and momentum into the acoustic field within the channel. According to simple acoustic theory, the instantaneous pressure pulse above the ambient pressure, p', measured at a distance r from a monopole sound source [39] is

$$p' = \frac{\rho_s}{4\pi r}\left[\frac{d}{dt}\left(\frac{dV}{dt}\right)\right]_{(t-t_a)} \tag{1}$$

Where dV/dt is the volumetric generation rate at the source, ρ_s is the density of the sound source, and t_a corresponds to the time taken for the pulse traveling from the source to the measured point r.

This expression is strictly valid only under the following assumptions. First, for it to be a truly monopole source, the length scale of the source should be small compared to its distance from the measured point. This means that Eq.

(1) applies better for a far-field sound pressure in a free space than in a confined space. Second, the small perturbation hypothesis is used during the formula deviation so compression and expansion associated with the wave are assumed isentropic. Eq. (1) becomes less justifiable in described circumstances with shocks or detonation involved. Other simplifications such as inviscid, adiabatic and one-dimensional flows are also included.

In this 2D simulation, the injection serves as a line source when extrapolated into the real three-dimensional case, which violates the first assumption. Since a high-speed jet is injected into such a confined space, the generation of a shock cannot be avoided. And this does not meet the isentropic condition mentioned above, either. However, even though the general assumptions are not completely satisfied, Eq. (1) still gives a qualitative description of the sound pressure p' as to be shown below.

Considering quasi-one-dimensional flows, the net volume generation rate from injection might be found by

$$\frac{dV}{dt} = U_s\, d_0 \sin\left(\frac{\pi}{\tau_0} t\right) \cos\theta * l_z \tag{2}$$

Where U_s is the magnitude of the total injection velocity, τ_0 is the injection period and l_z is the assumed Z-axis width of the three-dimensional chamber occupied by the injection. In this study, the downward injection angle θ is set 45 degrees as a constant. Inserting this into Eq. (1), it yields the eventual form of the sound pressure p' at a distance r and time t as

$$p'(r,t) = \frac{\rho_s U_s d_0}{4\tau_0 r} \cos\left[\frac{\pi}{\tau_0}(t - t_a)\right] \cos\theta\, l_z \quad \text{with } 0 \le t - t_a \le \tau_0 \tag{3}$$

Eq. (3) indicates that the sound pressure at the closed end before shock reflection when $r = L$ follows a half-cosine waveform and is proportional to the injection mass flux rate and inversely proportional to the injection duration and the channel length. Deduced from this expression, $p'(L,t)$ reaches its peak as the most initial perturbation arrives at the closed end at $t = t_a$. After that, the sound pressure decreases gradually to a negative value below the ambient pressure due to the expansion waves. Fig. 2 compares the simulated pressure at the closed end with the profile predicted by Eq. (3) with the amplitude of pressure in arbitrary units. It can be obtained that the profile of the

simulated end pressure fits well with a half-cosine shape qualitatively, especially in the former half part. Features with an initial pressure peak and thereafter a long-time decreasing track coincide with the model prediction. In the latter half, due to the inevitable generation of the non-isentropic shock in a confined space, a negative pressure predicted from the linear analysis is not encountered in the simulation data.

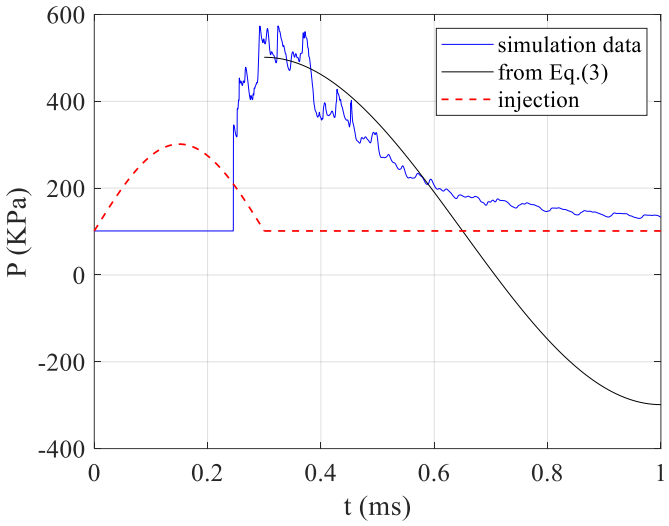

Fig. 2 Superposition of the injection characteristic and the comparison of end pressure profiles from simulation and the acoustic model

Eq. (3) has shown that the strength of the gas-dynamic shock is mainly dominated by the mass flow rate of injection with constant injection angle and duration. This means that the far-field flows can be regarded unchanged whether the jet is subsonic, sonic or supersonic if its mass flow rate is fixed. To achieve an identical mass flow rate, for a subsonic or sonic jet the supply pressure shall be large which makes it under-expanded most possibly while for a supersonic jet, with a relatively lower pressure it may be ideally expanded or over-expanded. We have tried earlier to employ an under-expanded sonic jet to simulate the injection in the experiments. However, due to the considerable difference between the injection and the ambient atmospheric pressure, p_i and p_0, an initial Riemann problem is established resulting in the inflow quantities with a superscript "--" (i.e., the pressure, temperature, velocity vectors and the injection angle) deviate significantly from the original injection quantities with a subscript "i", as illustrated

in Fig. 3. After careful inspection, we found that it is caused by the rarefaction waves blocking the inlet due to the misalignment between the normal direction of the inlet and the velocity vectors of the inflow, so the inflow experiences a pre-expansion immediately as it is ejected from the nozzle. To avoid this tough physical problem, as an alternative, our simulations use a supersonic gaseous jet at the ambient pressure and temperature. Since little attention is paid to the shape and the inner structures of the jet in this work and by considering an instantaneous expansion as soon as the under-expanded jet gets released, this should be reasonable. Even in reality, a high-Mach inflow can be achieved by connecting the high-pressure pump with the inlet through a convergence-divergence nozzle (a Laval nozzle).

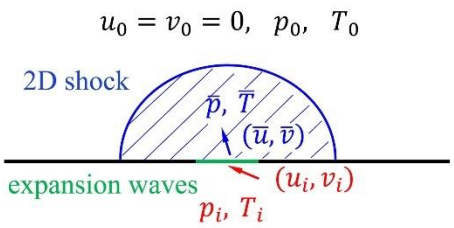

Fig. 3 Schematic diagram of the complex 2D Riemann problem at the inlet

Following simple acoustics theory, the amplitude of the planar wave activated in the channel follows a quarter-wave standing wave distribution, reaching its peak at the reflective wall and remaining approximately zero at the open end. So ideally, detonation would be expected to occur near the closed end where the detonation is most likely to be initiated by acoustic pulsing, quite like the principles of the pulse jet engine. Assuming that the acoustic wave propagates at the sonic speed, the required time for it to propagate from the injection point to the end wall is calculated as t_a = 0.3 ms, which corresponds exactly to the injection period τ_0. During this period, the detonable reactants should be delivered as deep as possible to the closed end in preparation for the subsequent end gas detonation here. By equaling the volume generation rate from injection to the required filling rate of the detonable mixtures in the channel,

$$\dot{V} = \frac{L_x * L_y}{t_a} = \overline{U_s d} = \frac{2}{\pi} U_s d_0 \tag{4}$$

the injection velocity U_s can be calculated as 897m/s, approximately 2 times the speed of sound, $c_s = 433m/s$. In the real situation the gas-dynamic shock propagates much faster than the sonic speed so in case, we specify an injection Mach stem of $Ma_i = 2.5$ corresponding to a total injection pressure of 1.7312 MPa, for more rapid filling. In this way, the reactants injected in each detonation cycle are sufficient to fill the entire length of the channel ideally if uniformly distributed, guaranteeing an adequate DDT run-up distance.

3. Numerical method

The governing equations in this simulation are the multi-species 2D Navier--Stokes equations with chemical reactions:

$$\frac{\partial \boldsymbol{U}}{\partial t} + \frac{\partial}{\partial x_j}\left(\boldsymbol{F}_j^{conv} - \boldsymbol{F}_j^{diff}\right) = S \tag{5}$$

$$\boldsymbol{U} = (\rho u_j, \rho e_t, \rho Y_k)^T \tag{6}$$

$$\boldsymbol{F}_j^{conv} = (\rho u_j u_i + p\delta_{ij}, u_j(\rho e_t + p), \rho Y_k u_j)^T \tag{7}$$

$$\boldsymbol{F}_j^{diff} = (\tau_{ij}, u_j\tau_{ij} - q_j, J_{k,j})^T \tag{8}$$

$$S = (0,0,\rho\dot{\omega}_k)^T \tag{9}$$

Where $\boldsymbol{U}$ is the state vector, $\boldsymbol{F}_j^{conv}$ and $\boldsymbol{F}_j^{diff}$ are the convective and diffusion fluxes, respectively, and S is the reaction source terms for $i, j \in \{1,2\}$ and $k = 1,2,\dots N$ (N is the number of species). The total internal energy e_t, shear stresses τ_{ij}, heat fluxes q_j and molecular diffusion fluxes $J_{k,j}$ are determined by

$$e_t = \frac{p}{\gamma-1} + \frac{u_j^2}{2} \tag{10}$$

$$\tau_{ij} = \mu\left(\frac{\partial u_i}{\partial x_j} + \frac{\partial u_j}{\partial x_i}\right) - \frac{2\mu}{3}\delta_{ij}\frac{\partial u_j}{\partial x_j} \tag{11}$$

$$q_j = -k\frac{\partial T}{\partial x_j} \tag{12}$$

$$J_{k,j} = D_k(\rho\frac{\partial Y_k}{\partial x_j}) \tag{13}$$

Where γ is the specific heat ratio, μ is the mixture viscosity, k is the thermal conductivity and D_k are the

molecular diffusion coefficients.

A detailed chemistry model with 13 species and 27 steps presented by Burke [53] for high-pressure combustion is employed to better capture the compressible flame and autoignition phenomenon before the onset of detonation. For the transport properties, μ is obtained by a semi-empirical model [40] and k is obtained by a simple method that applies a combined mixing rule [41]. D_k are calculated to be inversely proportional to the mixture pressure with the Wilke multi-component diffusion model. The effective Lewis number Le_{eff} [42] is calculated to evaluate the diffusive flame instabilities. Table 1 lists the initial transport properties of the mixture and the calculated flame and detonation parameters. By solving the one-dimensional premixed adiabatic flame, the laminar flame thickness is obtained from $\delta = (T_{ad,0} - T_o)/(dT/dx)_{max}$.

The open-source Adaptive Mesh Refinement Object-oriented C++ (AMROC) program [43-44] is employed in this work to capture the high-gradient regions dynamically. For numerical schemes, the time-operator splitting method [45] is employed to decouple the transport equations and the reactive source terms. The convective terms of the Navier-Stokes equations are discretized by a hybrid Roe-Harten-Lax-Van leer (Roe-HLL) Riemann solver with the fluxes reconstructed by the second-order accuracy MUSCL-TVD scheme and the Minmod limiter. The diffusion terms are discretized by the second-order accurate central difference scheme. The fourth-order accurate semi-implicit GRK4A method [46] is employed for the integration of the stiff reactive source terms. A MUSCL-Hancock method [47] is employed for second-order accuracy explicit time integration. Meanwhile, a dynamic time-step method is employed to guarantee a global CFL number of 0.8.

The initial size of the calculation mesh is $0.25mm \times 0.25mm$. Three calculation tests with 4-level, 5-level, and 6-level mesh refinement are conducted, corresponding to the highest resolution of 10.2, 20.4, and 30.6 Pts/δ (points per flame thickness), respectively. In both the 5- and 6-level cases, detonation is triggered by the exact same mechanism of a reflected acoustic shock interacting with the flame, although the location differs slightly. This is

because that turbulent combustion is intrinsically stochastic and highly dependent on the initial conditions as well as the grid size. In the 4-level case, local detonation is initiated before the shock--flame interaction during the propagation of the fast turbulent flame, due to higher numerical dissipation in a relatively coarse meshing. In all three cases, no local hot spots are observed to evolve spontaneously from the boundary layer to detonation, indicating that the influence of the grid resolution on the boundary-layer effects can be excluded. Moreover, prior work found that 5--10 grid cells per flame thickness is accurate enough to resolve the flame structure [48]. Consequently, the following results are all based on the 5-level refinement.

4. Results and discussion

4.1 Overview of the rapid DDT process

Fig. 4 depicts the critical phenomenon of the whole rapid DDT process with the jet installed 2cm downstream of the open end. To initiate the flame, a weak spark (i.e., p_k = 1 atm and T_k = 3000 K) is set slightly upstream of the ejecting jet to take advantage of the jet turbulence. The promotion of the jet turbulence on DDT in experiments was highlighted by Lu [38] and is discussed in Sec. 4.2 in detail. As can be seen, a turbulent flame forms rapidly after the flame–jet interaction, propagating toward the closed end with a highly distorted surface. The gas-dynamic shock, after reflecting from the solid wall, interacts back with the flame and triggers the local detonation at about 0.35 ms. This case has been confirmed through a large number of repetitive tests to always lead to a detonation by the similar flame-shock interaction mechanism, although the time taken for the flame passing through the ejecting jet differs due to the randomness and uncertainty of turbulence which dominates the prior flame jet interaction. The initiation of detonation relies little on the boundary-layer effects as discussed in the convergence analysis, which is quite different from the scenarios in submillimeter-scale tubes

Previous experiments [49] have reported a DDT preparation distance of 60cm–70 cm for a stoichiometric

hydrogen-oxygen mixture in a centimeter-scale tube under the initial conditions of 1 atm and 311 K. And it takes a much longer distance for DDT to occur in mixtures composed with hydrogen and air/nitrogen-doped oxidizers [50]. It is kind of unforeseeable that by adopting a different injecting and igniting strategy, a robust DDT can be acquired within such a short distance in this 2D simulation. So the main text in the following sections is to explain the physical mechanisms clearly. As reported by Cooper [6] and Wintenberger [51], the difference of impulse generated by DDT or by direct detonation in experiments is within 10%–15% of each other, regardless of the DDT direction as long as the detonation occurs within the tube. This gets proved again with the impulse yielded by integrating the closed-end pressure over time of this case comparable to traditional PDEs, which is also consistent with the experimental measurement [35].

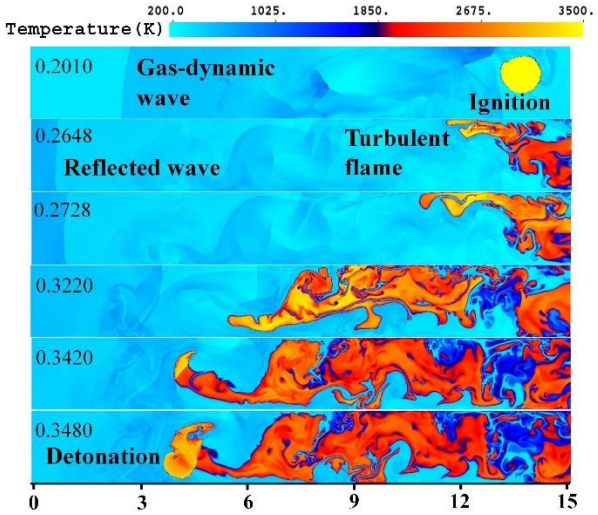

Fig. 4 2D Pseudo-color maps of the temperature illustrating a rapid DDT process. Times (ms) are given in the upper-left corner of each frame.

4.2 Generation of a CJ deflagration flame

The Chapman–Jouguet (CJ) deflagration speed, $U_{CJ,F}$, is the theoretical maximum speed for a self-accelerating flame allowed by conservation laws. Exceeding the CJ deflagration speed which is equal to the sonic speed in the hot products [52], the flame will transition into a choking (or fast turbulent, compressible) regime with precursor

compression waves generated ahead of it. This regime is important because it prepares the necessary conditions for detonation initiation.

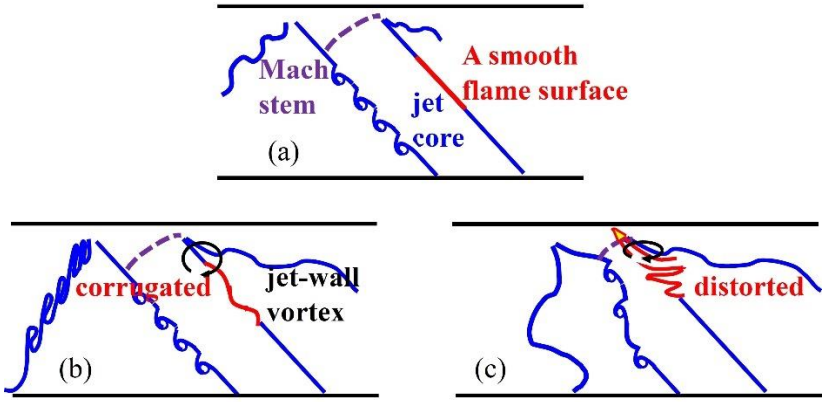

Fig. 5 Schematic diagram of jet flame interaction

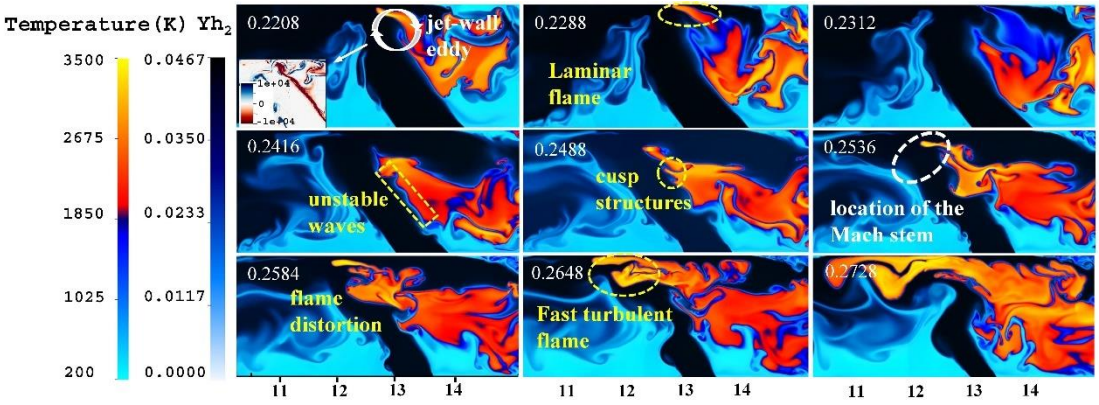

Fig. 6 Superposition of the temperature and the mass fraction of H_2 illustrating the flame regime transition

As mentioned in the last section, due to the complicated nature of turbulence the initiated flame passes the high-speed jet in slightly different characteristics among different tests. Fig. 5 describes schematically the most typical mode of the generation of a compressible flame, combined with the detailed simulation results in Fig. 6. Firstly, with the high-inertia jet continuously impinging on the upper wall, a large-scale vortex named as the "jet-wall vortex (**JWV**)" is produced at the jet bifurcation corner. At about $t = 0.22\,ms$, the **JWV** attempts earlier to entrain the smooth flame surface, which is stabilized on the shear layer of the unreacted jet, to pass through the highly turbulent

region controlled by jet impingement. This was not easy because traditional fluidic obstacles with a length scale, l_f are usually sufficiently smaller than the hydrodynamic scale of the flame, l_h, that they can easily penetrate deep into the flame domain and effectively disrupt the flame. However, the characteristic scale of the **JWV**, l_{JWV}, related to the size of the unreacted jet, is comparable to the size of the flame head with the propagation channel of flame greatly compressed by jet impingement. Consequently, the **JWV** cannot effectively disrupt the flame leaving it still in a laminar character around 0.2288 ms Then the convective heat loss introduced by the strong turbulence prevails and destroys the flame at $t = 0.2312\, ms$.

It is not until $t = 0.2416\, ms$ that flow or flame instabilities begin to induce out small disturbances on the smooth surface of the flame, in the form of unstable corrugated waves as clearly depicted in Fig. 5(b). As shown in the middle three frames in Fig. 6, these tiny disturbances got stretched in the axial direction developing into as cusp-like structures that penetrate deep into the flame surface, once again due to the entrainment of the jet-wall vortex and also the co-extrusion between the bulk and bifurcation of the unreacted jet. This mechanism, differing from the traditionally reported flame–turbulence interaction [7-8], is considered to be the main contributor to the flame regime transition in this case. As the flame meets with the Mach stem located in the jet core shown in Fig. 5(c), it is further accelerated by the increased density of the frontal reactants. Eventually, a fast turbulent flame, characterized with brushes induced by the Rayleigh-Taylor (RT) instabilities, successfully passes through the high-speed jet in the last three frames of Fig. 6. A choked flame is formed qualitatively indicated through the generation of compression waves, which swing the downstream-ejecting jet upstream to the chamber exit. Fig. 7 displays the displacement speed of the flame tip, s_T, nondimensionalized by the adiabatic sonic speed, $c_{ad,0} = \sqrt{\gamma_2 R_2 T_{ad,0}}$, in the laboratory frame with its axial position, x, nondimensionalized by the channel length L. The adiabatic sonic speed is calculated from

$$c_{ad,0} = \sqrt{\gamma_2 R_2 T_{ad,0}} \tag{14}$$

Where γ_2, R_2 are determined from the chemical equilibrium state holding the pressure fixed using the reaction

kinetics by Burke [53]. The horizontal shaded-gray zones cover the range of the CJ deflagration speed, $U_{CJ,f} \approx 1.02 - 1.12\, c_{ad,0}$, due to a slightly elevated product temperature and pressure, T'_{ad} and p'_{ad}, by the incident shock compression and the CJ detonation speed, $U_{CJ,d} \approx 1.94\, c_{ad,0}$, which remains basically unchanged, respectively. It can be seen that, after ignition, the flame is quickly accelerated to $U_{CJ,f}$, quantitatively proving again the choking regime. Plus, an overdriven detonation is also confirmed from Fig. 7 later in the flame propagation with a flame speed significantly higher than the CJ detonation speed, $U_{CJ,d}$, before it degenerates into a supersonic flame due to fuel deficiency.

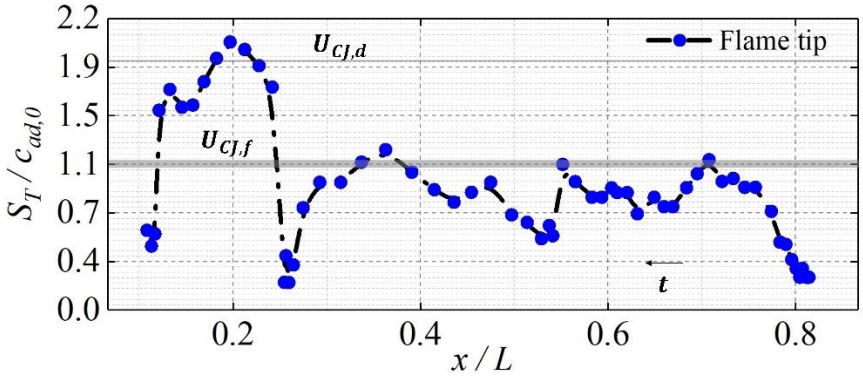

Fig. 7 Flame speed relative to the laboratory frame with the position of the flame tip

4.3 Detonation initiation by a shock-flame interaction

A direct numerical simulation study has illustrated that a flame, once in the choking regime, can quickly transition to a detonation in a high-intensity turbulent flow field. Nevertheless, in the absence of strong turbulence, this spontaneous process through wave generation and amplification usually requires a much longer distance and time. In this study, however, once meeting the reflected shock the deflagrative flame is transitioned immediately to a detonation after a considerable opposed convective transportation as shown in Fig. 7.

Detail of this complex are shown in Fig. 8. As can be seen, the reflected shock is greatly bifurcated as it passes over the flame due to the difference in propagation speed between the product and reactant inside and outside the flame. This generates a local Mach stem in the junction between the bifurcated shocks. At a certain point, the

inherently unstable bifurcated shock induces an auto-ignition by compression of the local Mach stem. With the shock-front unreacted mixtures in a pre-compressed condition at $p_1 = 270\,KPa$, its corresponding pressure passing through the Mach stem is measured as $p_2 = 2\,MPa$, significantly lower than the VN pressure p_{VN} of 4.76MPa of the CJ detonation. This implies that the Mach stem cannot directly initiate a detonation through adiabatic compression. Instead, due to the presence of a spatial reactivity gradient, the induced hot spot expands continuously eventually evolving into a detonation through Zel'dovich's gradient mechanism [54] or the shock wave amplification by coherent energy release (SWACER) mechanism [55]. Fig. 9 further illustrates this mechanism from the evolution of pressure and temperature profiles in a control volume V along the wave propagation direction during $t = 345.052\,\mu s - 346.682\,\mu s$. The averaged propagation speed of the spontaneous reaction wave, u_w, is calculated as just one-tenth of the CJ detonation speed $U_{CJ,d}$. As can be seen, the initial induction length between the shock and reaction fronts x_0 of about 0.2mm is much large than that of compressed a CJ detonation x_d calculated as 0.044 mm by the Shepherd's Shock and Detonation Toolbox (SDToolbox) [56]. Subsequently, a nonlinear growth in the wave strength prevails, accompanied by a significant decrease in the ignition length and pressure amplification until the emergence of the detonation transition point. At this critical point, the post-wave pressure finally exceeds p_{VN}, indicating the formation of an overdriven detonation, which is consistent with the illustration from Fig. 8.

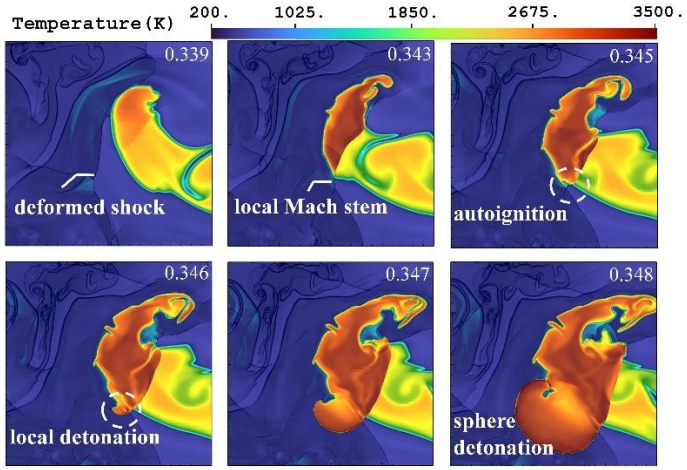

Fig. 8 2D Pseudo-color maps of the temperature illustrating the onset of detonation

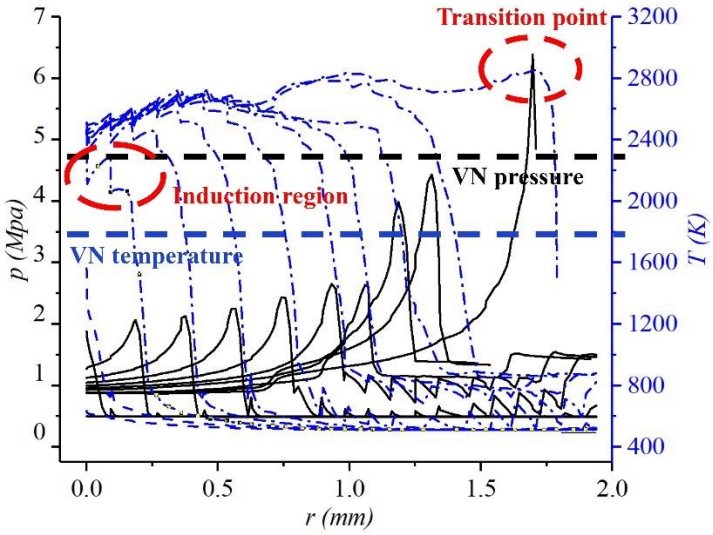

Fig. 9 Time sequences of pressure and temperature profiles illustrating the SWACER mechanism

4.4 Auto-ignitive front propagation by chemical physics analysis

To evaluate the strength of the gas-dynamic shock, a pure injection case without combustion was conducted for some preliminary conclusions. As shown in Fig. 10(1), due to the interaction with the incident boundary layers, the reflected shock exhibits a mild bifurcative characteristic near the walls with the bulk of the shock remaining planar. An obvious stagnation bubble is formed behind the shock foot, inducing complicated shock bifurcation structures. By extracting the post-shock quantities of ten points distributed uniformly in the Y-axis direction behind the reflected shock, the local ignition delay time gets calculated which determines the ignitive behavior of the fresh reactants. The post-shock temperatures of these points are found to fall in the scope between 540K and 660K with a relatively lower value emerging behind the shock foot outside the bubble, and the pressures are situated in the range between 70KPa and 120KPa. Using the constant-volume reactor model [57], as seen in Fig. 10(2), the ignition delay time τ_i in this case is calculated at the order of ~100 s, which is much larger than the residence time of the reflected shock τ_{res}. In other words, the gas-dynamic shock driven by the fuel injection is not strong enough to directly induce the autoignition here, which makes it quite different from the scenarios studied in the shock tube kinetic experiments.

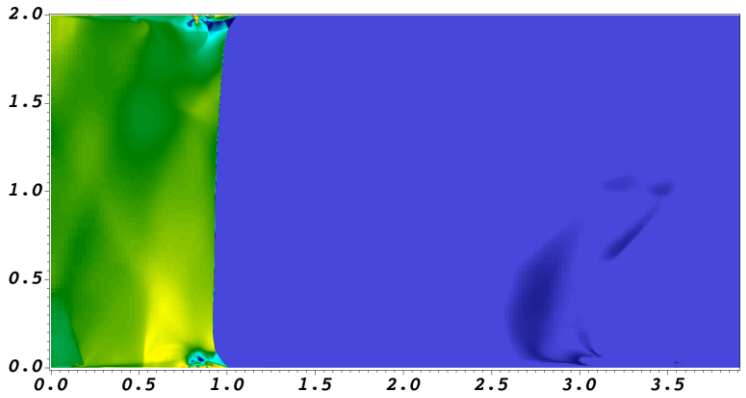

(a)

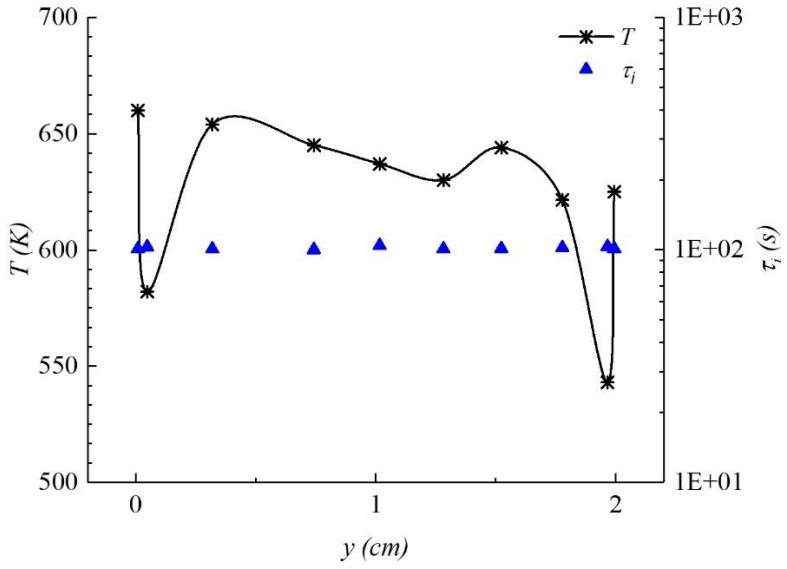

(b)

Fig. 10 (a) A mild shock bifurcation structure in the pure-injection case, (b) Vertical distribution of the post-shock temperature and ignition delay time

The above preliminary discussion implies that during the rapid DDT process, the thermal dynamics of the flame and the shock-flame interaction play an indispensable role in the eventual detonation initiation. In Sec. 4.3, we have demonstrated from the perspective of physical dynamics that the emergence of a local Mach stem by shock-flame intersection results in the local autoignition, which then develops into an explosion by a sequence of reaction front acceleration and pressure amplification through the SWACER mechanism. Here, further quantitative analysis from the perspective of chemical physics is presented by using a classic dimensionless number ξ [58, 61], defined by the

ratio of the acoustic velocity to the velocity of the auto-ignitive reaction front as

$$\xi = a/u_a \tag{15}$$

Where the velocity of the auto-ignitive reaction front is given by

$$u_a = \frac{\partial r}{\partial \tau_i} = (\frac{\partial \tau_i}{\partial T})^{-1}(\frac{\partial T}{\partial r})^{-1} \tag{16}$$

ξ illustrates the competition between the physical and chemical propagation speed. Following Zel'dovich [59], $\xi < 1$ yields a supersonic deflagration combustion mode with the autoignition front running fast than the acoustic wave. When ξ approaches unity, the autoignition front slows down and coincides with the acoustic wave thus a spontaneous pressure amplification in resonance with the energy release can be achieved in the form of a developing detonation. As it further decreases, the autoignition front gradually loses the suitable phase with the acoustic wave and thus manifests itself as a subsonic deflagration flame until u_a equals to the laminar flame speed u_l when the diffusion effects dominate the propagation of the reaction front.

Experimental results [12, 62] show that for hydrogen-air mixtures the logarithm of ignition delay time, $\ln\tau$, exhibits a near-linear relationship with the inverse of the temperature, $1/T$ so that the ignition delay time τ can be expressed in an Arrhenius form as

$$\tau_i = Aexp(\frac{E}{RT}) \tag{17}$$

Assuming the ignition delay time monotonically changes with the temperature under a fixed pressure and equivalence ratio, the pre-exponential factor A as a constant quantity can be easily determined from the zero-dimensional reactor model. In this case, the pressure is chosen to be 1MPa as a typical post-shock pressure of the nearly homogeneous unburned mixtures behind the Mach stem and the equivalence ratio is 1.0.

Substituting Eq. (17) into Eq. (16), the eventual form of u_a is expressed as

$$u_a = -(\frac{T^2}{\tau_i E/R})(\frac{\partial T}{\partial r})^{-1} \tag{18}$$

The global activation energy E can be calculated from

$$E = -2R\left(\frac{\partial(\ln(\rho_0 S_L))}{\partial(1/T_{ad})}\right)_{p_0,\phi} \quad (19)$$

as depicted by Yang and Radulescu [63] in detail. Here, we simply follow Bradley's statement [60] that for H_2-air mixtures the global activation temperature E/R is 22480 K.

Thus, the propagation speed of the auto-ignitive front would be obtained if knowing the local temperature, ignition delay time and the temperature gradient. Inserting it into Eq. (15), the dimensionless number ξ can be availed by

$$\xi = \frac{\mathrm{a}}{u_a} = -\tau_i(E/RT^2)(\partial T/\partial r)a \quad (20)$$

Fig. 8 and 9 have illustrated the dynamic transition mechanism by pressure amplification reinforced by the coherent energy release. In this section, this process is further presented from a more micro perspective by the competition between the chemical and acoustic velocity scales. According to Eq. (18) and the assumption above it, 2D Pseudo-color cloud maps illustrating u_a right before detonation can be obtained in Fig. 11. In Fig. 11, two distinct regions can be observed: the red region refers to the combustion products while the dark-blue region represents the unburned reactants, and separating them is the diffusive flame front depicted by a black solid line. Since we have assumed an equivalence ratio of 1.0 globally, to make our analysis meaningful, the unburnt region located below the diffusion profile shall be focused on in the following discussion.

As discussed in Sec. 4.3, when the reflected shock passed by the turbulent flame, a local Mach stem was formed by shock bifurcation due to the spatial differences in shock propagating speed in the hot and cold mixtures. Then autoignition is induced behind the Mach stem. The compression of the Mach stem is manifested as a glowing region shown in Fig. 11. Besides, the increased molecular concentration of the active radicals diffused by the flame should also contribute to the emergence of autoignition, which is not considered here. As extracted from Fig. 11 (1), the corresponding velocity of the chemical front u_a reaches up to 50 m/s, dozens of the laminar flame speed and several times lower than the sound speed. This implies that the combustion at the reaction front is still in a slow deflagration

mode. At this instant, the reaction front remains completely uncoupled from the shock front. As the spontaneous pressure waves emanating from the reactive front consistently compress the mixtures inside the induction region, the temperature is further increased shortening the ignition delay here. In Fig. 11(2) at t = 0.345 ms, a finger-like burnt peninsula is observed generated from the rapid consumption by the reaction front. Moreover, part of the reaction front begins to connect with the Mach stem with a significantly increased propagation velocity of about 387 m/s, pretty close to the acoustic speed. After that, a quick explosion emerges indicating the combustion transitions successfully from a deflagration mode to a detonation mode, as has been illustrated in Fig. 8 and 9.

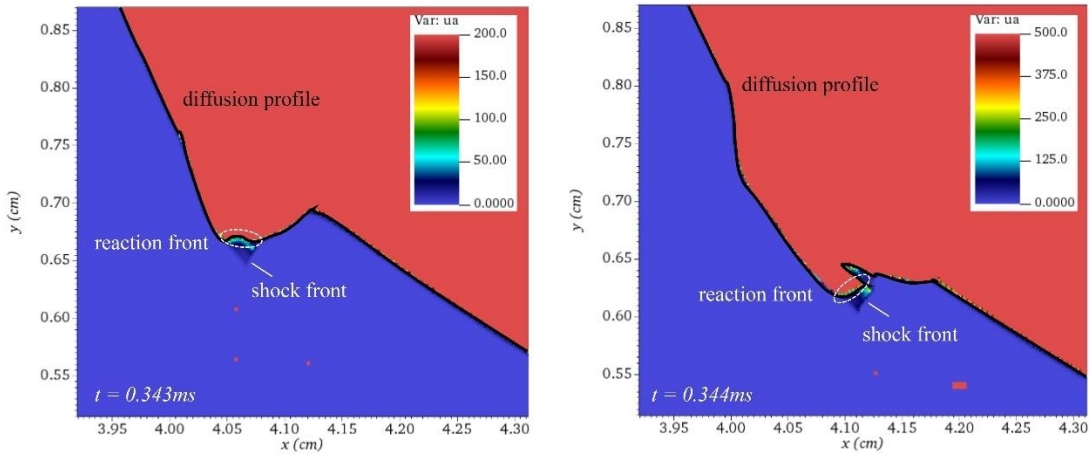

Fig. 11 2D Pseudo-color maps of the u_a illustrating the evolution of the auto-ignitive reaction front

Fig. 12 shows the evolution of the dimensionless criterion ξ and the ignition delay time τ during the transition. Due to the nearly instantaneous characteristic of the transition process, only three typical time instants got captured. Despite that, it can still be concluded that both ξ and τ change exponentially with time, which corresponds intrinsically to the non-linear nature of the acoustic-chemistry coherence. At t = 0.343 ms when the local Mach stem first emerged, the ignition delay τ_i was initially increased to about 4.15 ms. The corresponding auto-ignitive front behaves just more like a diffusion front with a propagation velocity of 1.58 m/s, pretty close to the laminar flame speed with the $\xi \ll 1$. Until right before the onset of detonation at the time of 0.345 ms, the reaction front reaches a typical velocity of 387 m/s pretty close to the acoustic velocity of 550 m/s. At this time the ξ equals about 0.7 corresponding to the τ_i of about 4.87e^{-02} ms. The dimensionless criterion ξ gives a good prediction of the

combustion mode of the reaction front, especially for a detonation regime when this number approaches 1.

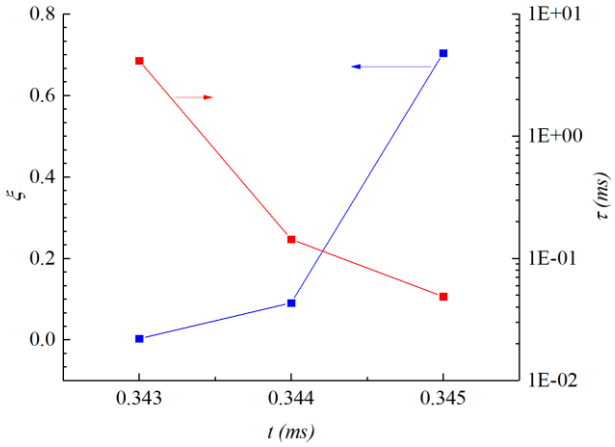

Fig. 12 Time-dependent variation of ξ and τ_i illustrating the combustion mode transition

5. Conclusion

The work describes numerically a rapid DDT process in a high-frequency pulse detonation rocket engine. By injecting reactants near the open end toward the closed end, a gas-dynamic shock is generated and high-intensity turbulence is produced by the impingement of the jet. This process is started from a weak ignition set appropriately upstream of the jet. Entrained by the clockwise-rotating vortex near the upper wall, the laminar flame is accelerated rapidly to a choking regime with precursor waves generated. The gas-dynamic shock, after reflecting from the end wall, interacts with the propagating flame and thus induces autoignition around the flame tip. The hot spot, as analyzed from the perspective of fluid dynamics, evolves into a detonation through the SWACER mechanism. During the transition, a predictive criterion is utilized to capture different combustion modes by the competition between the acoustic and chemical propagation speed. It is proved to give a good prediction of the combustion mode of the reaction front, especially for a detonation regime when this number approaches 1.0.

Acknowledgment

This work is supported by the National Natural Science Foundation of China (No. 11702323 and No. 12202487).

References

1K. Kailasanath, AIAA journal 38, 1698 (2000).

2K. Kailasanath, AIAA journal 41, 145 (2003).

3G. D. Roy, S. M. Frolov, A. A. Borisov, and D. W. Netzer, Progress in Energy and Combustion Science 30, 545 (2004).

4G. B. Goodwin, R. W. Houim, E. S. Oran, Combustion and Flame 173, 16 (2016).

5G. B. Goodwin, R. W. Houim, E. S. Oran, Proceedings of the combustion institute 36, 2717 (2017).

6M. Cooper, S. Jackson, J. Austin, E. Wintenberger, and J. E. Shepherd, Journal of propulsion and power 18, 1033 (2002).

7J. P. McGarry, K. A. Ahmed, Combustion and Flame 176, 439 (2017).

8B. Knox, D. Forliti, C. Stevens, J. Hoke, and F. Schauer, 49th AIAA aerospace sciences meeting including the new horizons forum and aerospace exposition 587, (2011).

9R. W. Houim, A. Ozgen, E. S. Oran, Combustion Theory and Modelling 20, 1068 (2016).

10D. Liu, Z. Liu, H. Xiao, International Journal of Hydrogen Energy 47, 11052 (2022).

11H. D. Ng, 2005.

12K. Fieweger, R. Blumenthal, G. Adomeit, Combustion and Flame 109, 599 (1997).

13F. L. Dryer, M. Chaos, Combustion and Flame 152, 293 (2008).

14S. M. Walton, X. He, B. T. Zigler, and A. Atreya, Combustion and Flame 150, 246 (2007).

15H. Yang, M. I. Radulescu, Journal of Fluid Mechanics 923 (2021).

16H. Yamashita, J. Kasahara, Y. Sugiyama, and A. Matsuo, Combustion and flame 159, 2954 (2012).

17K. P. Grogan, M. Ihme, Proceedings of the Combustion Institute 36, 2927 (2017).

18K. P. Grogan, M. Ihme, Proceedings of the Combustion Institute 35, 2181 (2015).

19H. Xiao, R. W. Houim, E. S. Oran, Proceedings of the Combustion Institute 36, 1577 (2017).

20O. J. Teerling, A. C. McIntosh, J. Brindley, and V. H. Y. Tam, Proceedings of the Combustion Institute 30, 1733 (2005).

21A. Y. Poludnenko, Physics of Fluids 27, 014106 (2015).

22J. Zhao, L. Zhou, X. Zhang, K. Li, and H. Wei, Combustion and Flame 230, 111451 (2021).

23J. Zhao, L. Zhou, K. Li, X. Zhang, J. Pan, R. Chen and H. Wei, Combustion and Flame 222, 48 (2020).

24L. Zhou, D. Gao, J. Zhao, H. Wei, X. Zhang, Z. Xu, and R. Chen, Combustion and Flame 191, 453 (2018).

25H. Wei, X. Zhang, H. Zeng, R. Deiterding, J. Pan, and L. Zhou, Physics of Fluids 31, 076106 (2019).

26V. N. Gamezo, A. M. Khokhlov, E. S. Oran, Combustion and flame 126, 1810 (2001).

27A. M. Khokhlov, E. S. Oran, G. O, Combustion and flame 117, 323 (1999).

28A. M. Khokhlov, E. S. Oran, Combustion and Flame 119, 400 (1999).

29A. D. Cutler, G. C. Harding, G. S. Diskin, AIAA journal51, 809 (2013).

30F. Ma, J. Y. Choi, V. Yang, Journal of propulsion and power 21, 512 (2005)

31F. Ma, Y. Wu, J. Y. Choi, and V. Yang, 41st Aerospace Sciences Meeting and Exhibit 1168, (2003).

32W. Lu, W. Fan, K. Wang, Q. Zhang and Y. Chi. Operation of a liquid-fueled and valveless pulse detonation rocket engine at high frequency[J]. Proceedings of the Combustion Institute 36, 2657 (2017).

33A. Cutler, B. Beck, J. Wilkes, J. Drummond, D. Alderfer, and P. Danehy, 43rd AIAA Aerospace Sciences Meeting and Exhibit 1084, (2005).

34A. Cutler, J. Drummond, 44th AIAA Aerospace Sciences Meeting and Exhibit 555, (2006).

35N. Nguyen, A. Cutler, 44th AIAA/ASME/SAE/ASEE Joint Propulsion Conference & Exhibit 4690, (2008).

36A. Cutler, 44th AIAA/ASME/SAE/ASEE Joint Propulsion Conference & Exhibit 4691, (2008).

37A. D. Cutler, AIAA journal 49, 1943 (2011).

38W. Lu, K. Wang, Q. Zhang, Y. Wang, and W. Fan, Proceedings of the Institution of Mechanical Engineers, Part G: Journal of Aerospace Engineering 230, 886 (2016).

39I. R. Hurle, R. B. Price, T. M. Sugden, and A. Thomas, Proceedings of the Royal Society of London. Series A. Mathematical and Physical Sciences 303, 409 (1968).

40R. B. Bird, Appl. Mech. Rev. 55, R1-R4 (2002).

41S. Mathur, P. K. Tondon, S. C. Saxena, Molecular physics 12, 569 (1967).

42M. Matalon, C. Cui, J. K. Bechtold, Journal of fluid mechanics 487: 179 (2003).

43R. Deiterding, Dissertation. de, 2003.

44R. Deiterding, Computers and Structures 87, 769 (2009).

45N. N. Janenko, Die Zwischenschrittmethode zur Losung mehrdimensionaler Probleme der mathematischen Physik, Springer-Verlag, Berlin (1969).

46P. Kaps and P. Rentrop, Num. Math. 33, 55 (1979).

47B. van Leer, SIAM J. Sci. Stat. Comp. 5, 1 (1985).

48W. Zhao, J. Liang, R. Deiterding, X. Cai, and X. Wang, Physics of Fluids 33, 091704 (2021).

49L. E. Bollinger, M. C. Fong, R. Edse, ARS Journal 31, 588 (1961).

50L. E. Bollinger, AIAA Journal 2, 131 (1964).

51E. Wintenberger, J. M. Austin, M. Cooper, S. Jackson, and J. E. Shepherd, Journal of propulsion and power 19, 22 (2003).

52G. Ciccarelli, S. Dorofeev, Progress in energy and combustion science 34, 499 (2008).

53M. P. Burke, M. Chaos, Y. Ju, F. L. Dryer, and S. J. Klippenstein, International Journal of Chemical Kinetics 44,

444 (2012).

54Y. B. Zeldovich, Astro. Acta. 15, 313 (1970).

55J. H. Lee, R. Knystautas, N. Yoshikawa, Gasdynamics of Explosions and Reactive Systems. Pergamon 971, (1980).

56J. Lawson, J. Shepherd, California Institute of Technology, Pasadena, CA, (2019).

57G. B. Goodwin, D. Cantera, http://www.cantera.org (2002).

58X. J. Gu, D. R. Emerson, D. Bradley, Combustion and flame 133, 63 (2003).

59Y. B. Zeldovich, Combustion and Flame 39, 211 (1980).

60D. Bradley, G. T. Kalghatgi, Combustion and flame 156, 2307 (2009).

61L. Bates, D. Bradley, G. Paczko, and N. Peters, Combustion and Flame 166, 80 (2016).

62D. Bradley, C. Morley, X. J. Gu, and D. R. Emerson, SAE transactions 2679 (2002).

63H. Yang, M. I. Radulescu, Proceedings of the Combustion Institute 38, 3481 (2021).